Composites Part B 276 (2024) 111364

Contents lists available at ScienceDirect

Composites Part B

journal homepage: www.elsevier.com/locate/composites

Assessing the stress-transfer capability of mineral impregnated PBO yarns in a limestone calcined clay cement-based (LC^3) matrix

Cesare Signorini [a,*], Andrea Nobili [b], Marco Liebscher [a,b], Jitong Zhao [a], Ameer H. Ahmed [a], Thomas Köberle [a], Viktor Mechtcherine [a]

[a] Institute of Construction Materials, TU Dresden, Georg-Schumann-Str. 7, 01187 Dresden, Germany
[b] Department of Engineering "Enzo Ferrari", University of Modena and Reggio Emilia, Modena, 41125, Italy

ARTICLE INFO

Keywords:
PBO yarns
Pull-out
Mineral impregnation
Analytical model

ABSTRACT

Technical textiles made of poly(p-phenylene-2,6-benzobisoxazole) (PBO) represent attractive candidates for strengthening and repairing damaged concrete and masonry structures, due to the outstanding durability and mechanical performance of PBO fibres. Similarly to their aramid counterparts, PBO fibres have proved very effective against dynamic and impact loading. In this contribution, the pull-out behaviour of PBO multifilament yarns embedded into a blended cement-based matrix is investigated, with particular reference to its stress-transfer capacity. In addition to the as-received PBO yarns, impregnation with a cement-based suspension, which can fully preserve the inorganic nature of the composite system, is also evaluated. Experimental results are presented and interpreted using a one-dimensional mechanical model. The findings indicate that mineral impregnation of the yarns provides a 40% increase in the stress-transfer capacity with the matrix, corresponding to a halving of the anchoring length. These performance gains are also supported by a transition in the failure mechanism which shifts from friction-based pull-out to fibre rupture.

1. Introduction

Textile-reinforced concrete (TRC) has gained increasing popularity in recent decades, as a viable solution for strengthening and repairing existing reinforced concrete (RC) and masonry structures [1–3]. In fact, TRC features extreme versatility and fine-tunable design, combined with high damage tolerance and acceptable thermal stability [4]. Recently, poly(p-phenylene-2,6-benzobisoxazole) (PBO) has attracted attention as a constitutive material for high-performance woven textiles in TRC composites. PBO is a relatively modern synthetic thermosetting polymer, first produced by Toyobo in the 1980s under the trade name of Zylon®. Although the chemical composition of PBO is similar to that of aramid, PBO fibres feature exceptional tensile strength, about 60% and 25% higher than that of aramid and of carbon, respectively. Another important advantage of PBO lies in its structure, which consists of highly oriented microfibrils having diameter of 10–50 nm and capillary microvoids [5], resulting in light weight (about 1.55 g/cm^3) and high stiffness. For these reasons, PBO fibres are also attractive in strengthening applications against highly dynamic loading regimes [6]. In addition, the mechanical performance of PBO remains remarkably stable under adverse environmental conditions, as demonstrated by accelerated ageing investigations of composite systems exposed to aggressive agents [7,8] and high temperatures [9]. On the downside, the cost of PBO fibres is higher than that of other kinds of high-performance fibres, making them suitable only for niche applications.

In the field of structural retrofitting, PBO-TRC systems have been extensively investigated in the last decade as strengthening elements either to improve the ductility of concrete columns under compression, where high stiffness plays a key role [10,11], or to enhance the load-bearing capacity of RC beams [12,13]. In this context, Di Tommaso et al. [14] highlighted the improved damage tolerance achieved by PBO-TRC compared to carbon fabric-reinforced polymers (C-FRP). The adoption of PBO-TRC has also been reported in the context of the retrofitting of masonry structures, ranging from jacketing of pillars [15], extrados reinforcement of arched elements [16], panels, and hybrid historic infrastructures [17]. However, in many case studies addressing masonry structures, glass or basalt textiles are often preferred, because the relatively low residual performance of existing masonry represents the limiting factor and hence seldom justifies the use of ultra-high performance fibres.

As it is the case with many inorganic composites, the key design factor is the interaction between the PBO textile and the cement-based matrix. Earlier research has clearly documented that failure is largely governed by internal debonding and slippage of the textile, especially

* Corresponding author.
E-mail address: cesare.signorini@tu-dresden.de (C. Signorini).

https://doi.org/10.1016/j.compositesb.2024.111364
Received 4 October 2023; Received in revised form 4 March 2024; Accepted 5 March 2024
Available online 7 March 2024

for those without any pre-impregnation. Indeed, several studies have demonstrated the strong hydrophobic nature of PBO fibres [18], which greatly hinders chemical interaction with cementitious matrices. In this regard, recent studies aimed at evaluating the bond–slip behaviour of PBO textiles in TRC systems, provide evidence that the outstanding tensile potential of PBO fibres remains generally unexploited [19]. This is generally ascribed both to the low moisture regain of PBO fibres, i.e. 2%, and to the solid phase in the matrix being unable to fully adhere within the yarn bundles, which are insufficiently penetrated by the mortar, and are prone to the so-called telescopic failure [20]. Typically, this failure mode is characterised by large ductility and low exploitation rates in a generally inconsistent performance [21]. To overcome this important limitation, textiles are usually impregnated with external agents that can prevent telescopic failure by binding the filaments together and/or increase the chemical compatibility with hydraulic matrices, for example by depositing hydrophilic particles on the fibres surface. The former strategy generally encompasses the use of polymeric resins, e.g., epoxy, acrylate or styrene-butadiene [22–24], while the latter often relies on silica-based coatings [25–27]. Fibre functionalisation can also be pursued by other techniques, like chemical etching, plasma, or similar treatments [28,29]. Recently, inorganic impregnation techniques have been further investigated and developed [30], especially for carbon multifilament yarns, using geopolymer or cement-based fine-grained suspensions [31,32]. The major advantages of this innovative technique consist in the improved performance at high temperatures compared to polymeric impregnation [33,34], and the possibility of incorporating the impregnation stage into a highly automated and remotely controlled process, as shown by Mechtcherine et al. [35] and further developed by Liebscher et al. [36]. Indeed, the automated production line has been optimised by correlating the main technological parameters, such as the number and the deflection of the impregnation rollers, with the morphology and the mechanical behaviour of the finished carbon fibre yarn.

In this paper, the bond behaviour of PBO yarns, with and without cement-based pre-impregnation, embedded in a newly developed limestone calcined clay cement (LC^3) fine-grained mortar is experimentally assessed. A phenomenological analytical model is also proposed to describe the mechanisms that occur during the extraction of individual yarns from the matrix. This is a simple stress and friction model, developed along the lines originally presented by Kelly [37] and later generalised in many directions (see, among many others, Hutchinson and Jensen [38] and later on Sorzia et al. [39], Sorzia et al. [40] for single fibres embedded in a brittle matrix). In particular, it addresses some of the limitations of previous models as described in DiFrancia et al. [41], more specifically the need of a large number of parameters and their identification. Yet, the model aims to reproduce at least some of the main features of the stress distribution along the fibre, as described by Kerans and Parthasarathy [42] and DiFrancia [43]. The development of such friction-based models has paved the way for the holistic description of the tensile behaviour of a variety of textile-reinforced composites [44]. The effects of impregnation are clearly highlighted by this model both in terms of the maximum shear stress exchanged with the surrounding matrix and in terms of the reduction in extinction length.

2. Materials and methods

2.1. Raw materials

2.1.1. Fibres and impregnating agent

High modulus PBO yarns (Zylon®-HM) [45] are supplied in bobbins by Toyobo Co., Ltd., Japan, each yarn consisting of 332 filaments. The main physical properties, as declared by the manufacturer, are specified in Table 1.

Mineral impregnation of the PBO yarn is made possible by a low-viscosity cement-based slurry characterised by a high water-to-cement (w/c) ratio of 0.8. The binder is a blend of two highly refined grey cement and slag based matrices with different particle size distributions, commonly adopted for the preparation of injectable cement suspensions. The mix design for the cement-based impregnating agent is described in Table 2, which includes detailed information about the raw constituents.

Table 1
Physical and mechanical properties of the PBO yarns, according to the producer [45].

Property	Unit	Value
Filament count	dtex	1.7
Diameter of the fibres	μm	12[a]
Cross section of the single yarn, A_f	mm^2	0.04
Density	$g\,cm^{-3}$	1.56
Tensile strength	MPa	5800
Tensile modulus	GPa	270
Ultimate strain	mm/mm	0.25
Decomposition temperature	°C	650
Limiting Oxygen Index (LOI)	–	68

[a] Diameter according to Huang et al. [46].

First, water and microsilica are mixed with the first batch of naphthalene-sulfonate-based superplasticiser using a common immersion blender for 1 min. The two varieties of micro-cement powder are then gradually added, while stirring, until a homogeneous slurry is obtained. Eventually, a second batch of superplasticiser is added to the slurry to achieve high workability. The mixture is further homogenised by using an intensive disperser, i.e. a T50 digital ULTRA-TURRAX® equipped with an R50 stirring shaft and an IKA R1402 dissolver. This dispersion process is run for 1 min at a constant rotational speed of 7000 rpm.

2.1.2. Limestone calcined clay cement (LC^3) mortar

The embedding matrix is designed to attain moderate strength to better cope with the strengthening of deteriorated concrete and masonry members. The binder consists of a blend in which ordinary Portland cement (OPC) is partially replaced by limestone, calcined clay and dihydrate calcium sulphate (gypsum), in a weight ratio of 1:3. This formulation (hereafter labelled as LC^3-75) imparts a high degree of sustainability to the mortar due to the significant reduction in cement clinker [47,48]. The mixture is fully described in Table 3, and features a compressive strength of 24.5 MPa (±6%) [49].

2.2. Yarn impregnation

Impregnation of the unidirectional roving with the cement-based mineral suspension is undertaken in a continuous automated pultrusion line driven by a fully digitalised control system [35,50]. The production of mineral-impregnated PBO fibre (MPF) yarn element is realised by pulling and winding the roving on a large hexagonal motor-driven wheel and passing through three yarn-guiding levels, a motor-driven kiss-coater and an impregnation bath consisting of a Foulard system with five rollers, each with a diameter of 4.2 cm. Such a Foulard system ensures multiple deflection pressures on the roving to achieve effective penetration of the cement slurry into the bundle filaments. The MPF roving is then further shaped into an ellipsoidal cross-section by a conical plastic nozzle with an inner opening diameter of 2.3 mm (see Fig. 1). This final step entails the MPF cross-section with enhanced dimensional consistency and promotes alignment of the constituent fibres.

As a result, MPF yarns are more compact, with a diameter of 361 μm (±5%), as opposed to the diameter of 596 μm (±22%) of the loose as-received PBO yarn counterpart.

Fig. 2 compares the appearance of the as-received yarn and the impregnated MPF fibre.

Table 2
Composition of the cement-based suspension for mineral-impregnation of the PBO yarns (the dosages refer to 1 litre (1 dm^3) of suspension).

Property	Sort/Manufacturer	Density [g/cm^3]	Dosage [g/dm^3]
Micro-cement type 1	Mikrodur R-X/Dyckerhoff GmbH, DE	2.90	345.4
Micro-cement type 2	Mikrodur P-U/Dyckerhoff GmbH, DE	3.10	345.4
Microsilica suspension	Centrilit Fume SX/MC-Bauchemie, DE	1.38	345.4
Superplasticiser	MasterRheobuild 30/Master Builders Solutions, DE	1.08	13.0 + 18.1[a]
Water	–	1.00	493.3

[a] The two parts of superplasticiser were added at different stages.

Table 3
Composition of the cement-based mortar for embedding PBO yarns (the dosages refer to 1 litre (1 dm^3) of mortar).

Material	Sort/Manufacturer	Dosage [g/dm^3]
Cement	CEM I 52.5 R-SR3-NA/Holcim Technology Ltd., CH	286
Limestone	Saxodol 90 LE/sh minerals GmbH, DE	282
Calcined clay	Liapor GmbH & Co.KG., DE	564
Calcium sulphate	$CaSO_4 \cdot 2H_2O$/Grüssing GmbH, DE	9
Quartz Sand	d_{max} = 0.2 mm/BCS413, Strobel Quarzsand GmbH, DE	257
Superplasticiser	MG ACE 460/BASF, DE	8
Viscosity modifying agent	UW Compound-100/Sika AG, CH	4
w/b ratio	–	0.40

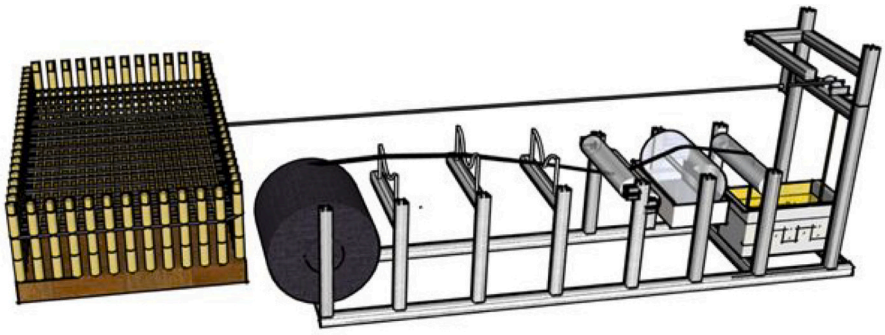

Fig. 1. Sketch of the automated processing line for continuous impregnation of the MPF reinforcement.

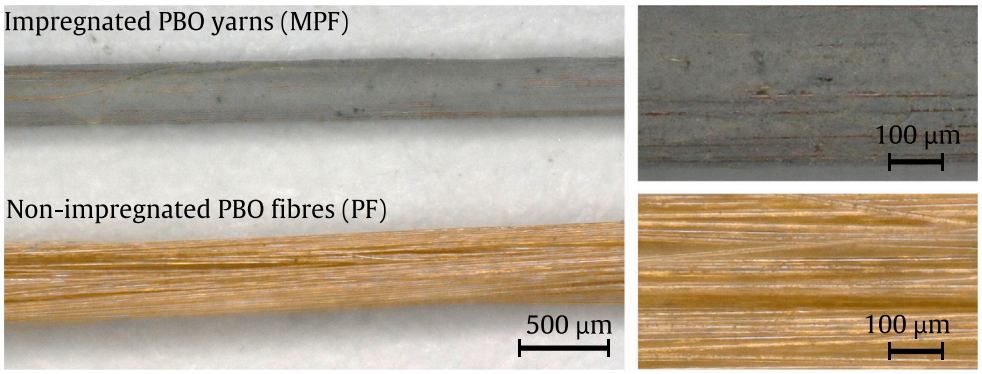

Fig. 2. Optical microscopy investigation of impregnated (top) and as-received (bottom) PBO yarns.

Straight MPF are left to cure in a wooden structure conceived for the assembly of biaxial textiles. Batches of MPF yarns are wrapped in a polyethylene foil and cured under standard conditions, namely 20°Celsius and 65% relative humidity (RH). For matrix reinforcement, individual MPF yarns are extracted from the mesh formwork after 28 days.

2.3. Specimen manufacturing

Mechanical characterisation of the PBO yarns is conducted by double sided pull-out tests. The geometry of the specimen is illustrated in Fig. 3a. A modular plastic formwork is used to cast the specimens in accordance with the protocol established by Butler et al. [51]. First, all the parts of the mould are lubricated with a silicone-based wax

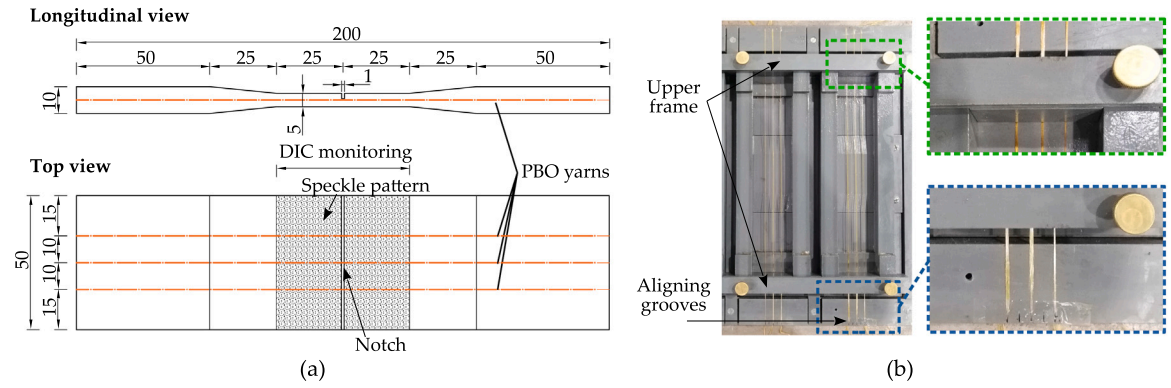

Fig. 3. (a) Double-sided pull-out specimen geometry (dimensions in [mm]), and (b) on-purpose modular plastic mould for manufacturing. Details on yarn alignment and fixation are also shown.

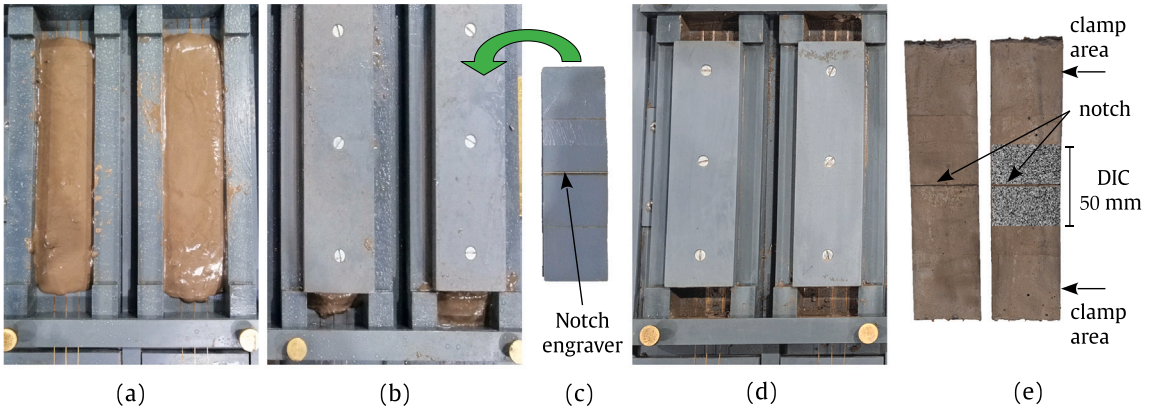

Fig. 4. Details of the manufacturing process of the specimens for double-sided pull-out tests.

to facilitate the removal of the specimens. The yarns are carefully placed in the bottom of the formwork using adhesive tape. Perfect alignment is ensured by the placement of groove guides. The yarns are then manually stretched and the upper plastic frame is screwed down tightly to keep them in place (see details in Fig. 3b). The inorganic matrix is produced by preliminary blending the solid phases in a Hobart mixer, before the addition of water and plasticiser, mixed previously. The mortar is then stirred for about 5 min, before being then carefully poured in the formwork and levelled with a scraper (see Fig. 4a). To impress the notch, a covering plastic piece with a protruding edge is gently pressed onto the top surface (see Fig. 4b-c). The depth of the notch is 1 mm. The excess mortar leaking out of the formwork is then carefully removed (see Fig. 4d). The samples are demoulded after 48 h and kept tightly wrapped in a plastic bag for the remaining 26 days (a total curing time of 28 days is here considered, see Fig. 4e).

2.4. Testing methods

Microscopic techniques are used to investigate the impregnation quality of the PBO yarns with the cement-based suspension. A VHX6000 video microscope (Keyence, DE) is used for lower magnifications and a scanning electron microscope (SEM), equipped with a Quanta 250 FEG microscope (FEI, USA) coupled with an EDX system for elemental mapping (Quantax 400, Bruker, DE), is used for higher magnifications on polished samples. Micro-computed tomography (μCT) is adopted to investigate the bond quality between the LC^3-75 matrix and the PBO yarns (CT-XPRESS, ProCon X-ray GmbH, Germany, coupled with X-Tom software). The X-ray voltage and current are 72 kV and 200 μA, respectively. The exposure time is 0.18 s, with three projections averaged to record the result.

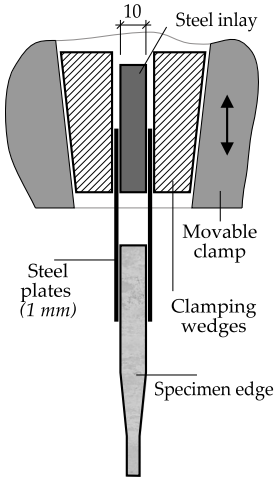

Fig. 5. Detail of the clamping system.
Source: adapted from Butler et al. [51].

Pull-out tests on composite specimens are carried out using a servo-hydraulic universal testing machine (UTM, Instron 8501, Instron GmbH, DE) equipped with a 100 kN load cell and operated under stroke control at a displacement rate of 0.05 mm/s. Specimens are clamped through wedge grips at both ends, where lateral steel plates are glued

Table 4
Pull-out test summary.

Label	Mortar	Yarn type	Number of yarns	Test speed	Repetitions
PF	LC^3-75	PBO, as received	3	0.05 mm/s	5
MPF	LC^3-75	PBO, cement-impregnated	3		5

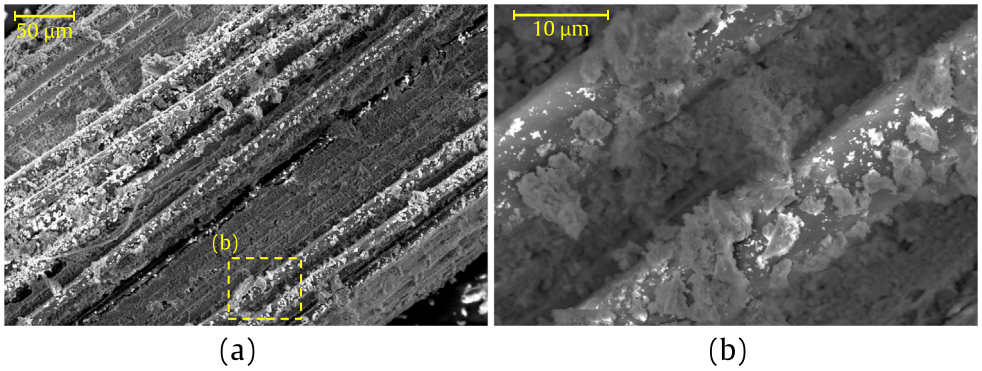

Fig. 6. SEM magnified views of longitudinally cut cement-impregnated PBO yarns: hydration products are clearly visible on the yarn surface.

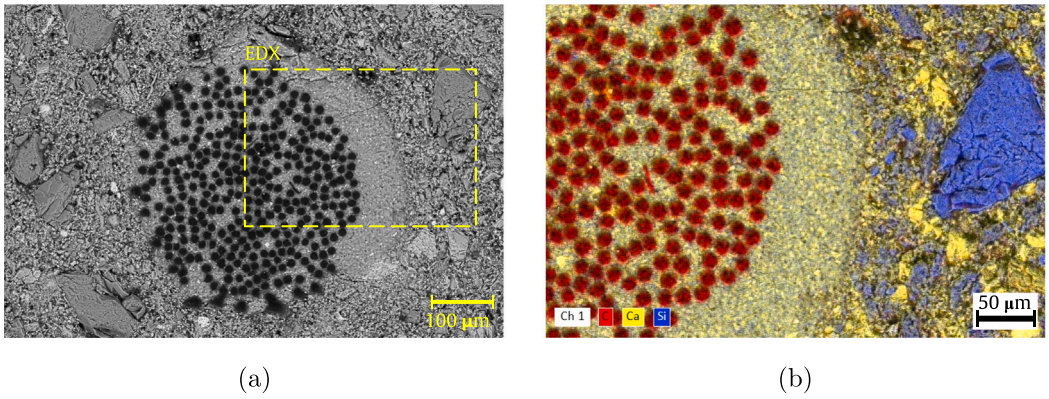

Fig. 7. SEM view and EDX map of the MPF yarn cross-section.

with strong epoxy resin to avoid concentrated loads on the matrix (see Fig. 5). The interested reader may refer to the previous studies [51] for a complete description of the test setup. Instead of monitoring the notch opening throughout the test with a system of linear variable differential transformers (LVDTs), Digital Image Correlation (DIC) is used (set of twin cameras with high intensity light source and post-processing by ARAMIS professional, GOM GmbH). The average displacement of the specimen half, which is connected to the movable part of the UTM is considered, net of any slippage measured on the other half of the specimen, i.e. connected to the fixed part of the UTM. The test matrix for this experimental programme is reported in Table 4.

3. Results and discussion

3.1. SEM analysis of the impregnation quality

Fig. 6 shows SEM images of longitudinally cut MPF yarns at two magnifications. It can clearly be noted that hydration products are formed which adhere to the fibre surface, suggesting a good adhesive affinity between the components.

Likewise, Fig. 7a reveals in cross-section the high quality of impregnation obtained at filament level. Indeed, the filaments are homogeneously distributed over the yarn area and slightly separated from each other by the cementitious suspension. This is nicely showcased in the corresponding EDX image with elemental mapping reported in Fig. 7b.

Here the individual components can be easily distinguished by the presence of carbon (C), calcium (Ca) and silicon (Si). Three distinct areas can be clearly identified, i.e. (i) the multifilament yarn, which is evenly impregnated by the cement-based suspension, (ii) the interlayer, which is still realised by the cement suspension and whose thickness may vary along the circumference, and (iii) the surrounding matrix, where the coarse quartzitic sand particles clearly stand out. Although the outer shape of the yarn, after being subjected to the automated impregnation process, generally closely resembles a circular shape, as documented in previous studies [36], the filament arrangement is slightly offset, possibly owing to the relatively low number of filaments. Nonetheless, the impregnating medium is still able to penetrate well into the roving and between the filaments.

3.2. Double sided pull-out tests

Fig. 8 plots the stress as a function of notch opening. The stress values are computed by normalising the applied load to the cross-sectional area of the PBO yarns in accordance with the prescriptions of the ACI 549 guidelines for externally bonded fabric-reinforced cementitious matrix (FRCM) composites [52].

The mechanical response of inorganic specimens in double sided pull-out tests is extensively discussed by Butler et al. [51]. Typically, three characteristic regimes can be identified: first, a stiff linear response is observed, highlighting the tensile properties of the matrix in the region close to the notch. Second, linearity is lost until a sudden stress drop occurs at notch brittle fracture. Third, a distinctive deformation-hardening response is developed, which reflects the progressive extraction (pull-out) of the yarns from the matrix. The test ends

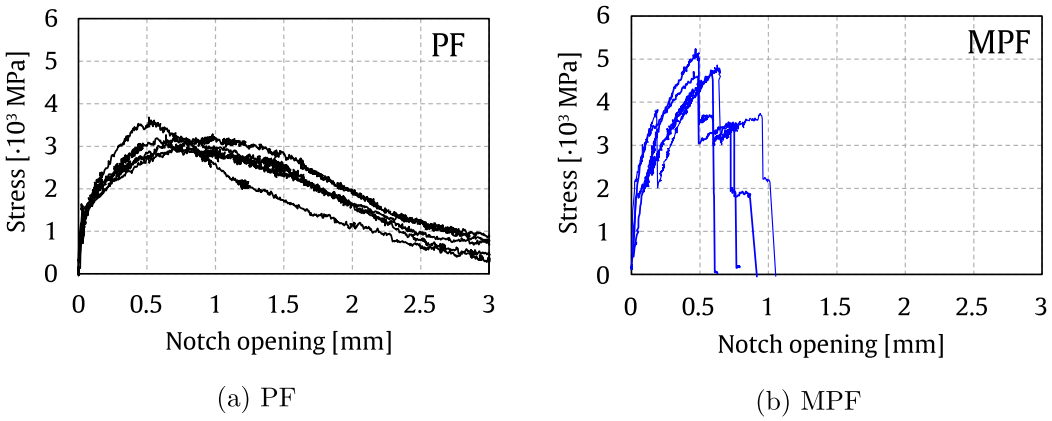

(a) PF (b) MPF

Fig. 8. Stress vs notch opening for non-impregnated (a) and impregnated (b) PBO yarns in pull-out testing.

Table 5
Summary of the pull-out tests (coefficients of variation are given in brackets).

Label	F_{max} [N]	σ_{max} [MPa]	Notch opening at F_{max} [mm]	ER [–]
PF	353 (±8%)	3269 (±8%)	0.64 (±14%)	0.56 (±8%)
MPF	528 (±5%)	4887 (±5%)	0.53 (±16%)	0.84 (±5%)

with either yarn failure or internal delamination at the yarn/matrix interface, followed by yarn extraction. By analogy with previous studies [30,51], it can be seen that both the first and second parts of the experimental curve are considerably influenced by the tensile properties of the matrix and they are only marginally represented when giving results in terms of notch opening. Consequently, only the third stage is really described in Fig. 8, and it is largely representative of the matrix-to-yarn interface response. Quantitatively, the performance of TRC is typically measured in terms of the *exploitation ratio* (*ER*). This dimensionless index expresses the extent of exploitation of the mechanical potential of the reinforcing fabric, and it is thus defined as

$$\mathrm{ER} = \frac{\sigma_{\max}}{f_{f,t}}$$

where $\sigma_{\max} = F/A_f$ is the maximum stress level achieved in the pull-out test, the applied load F being normalised to the yarn cross-section A_f, and $f_{f,t}$ is the tensile strength of the PBO fibres, equal to 5800 MPa according to the supplier (see Table 5).

The experimental curves for impregnated and non-impregnated fibres display different and distinct response patterns. Indeed, the bare PF samples consistently exhibit the same qualitative behaviour, consisting of a monotonically increasing hardening regime, that is followed by a softening response. The former accounts for progressive yarn/matrix debonding whereby the relevant bond stiffness, i.e. the slope of the ascending branch, progressively decreases until the ultimate bond stress is reached, cf. Section 4. This progressive loss of stiffness is ascribed to the bonded portion of the yarns moving deeper into the matrix, leaving some extra yarn length free to elongate (plus, possibly, fibre slippage). Then, when the yarn is completely free from the surrounding matrix, a friction-driven softening branch kicks in. In this particular test configuration, with a long embedment length, the residual stress level remains almost constant after a notch opening of about 3 mm, and it is caused by the slippage of the core filaments in the bundles [53]. Conversely, yarn impregnation (the MPF group) yields a completely different pattern. First, a stiffer response is clearly evident, likely due to the enhanced interface bond quality in combination with the bridging action exerted by the impregnating agent on the core fibres. The result is a significant increase in bond strength, albeit at the partial expense of ductility. This direct correlation between bundle impregnation and strength gain is also brought about by Slama et al. [54], although no pre-impregnation was performed on the multifilament yarns and the bond quality is somehow controlled by acting on the rheological properties of the matrix. Nevertheless, it is worth pointing out that, for MPF yarns, peak stress is reached while the stiffness of the stress curve remains positive, in contrast to the zero stiffness that is observed for PF counterparts at peak stress. This evidence suggests that MPF tensile rupture occurs slightly prior to full yarn delamination and consequently the bond quality is adequate to convey the full potential of the yarn. Such a finding is consistent with the relevant literature where impregnation is often able to revert failure from yarn pull-out to tensile rupture, see, e.g., Homoro et al. [55, Fig. 8 and Fig. 9].

The former failure mode is often associated with some extent of toughening due to slippage of the core filaments during the pull-out phase, which secures some stress transfer over a relatively wide displacement span. However, while this pseudo-frictional mechanism occurs, wide cracks develop in the TRC which are detrimental to durability and significantly impair the peak capacity of the system, that is incapable of fully harnessing the exceptional strength of the reinforcing fibres (e.g., PBO) [24,56,57]. In addition, telescopic failure is generally associated with lack of performance consistency, and its initiation is precipitated by several factors, many of which are related to small details in the manufacturing stage. On the other hand, if the failure occurs at the peak strength/strain of the PBO fibre, the designer can rely on a consistent behaviour, which results in less stringent safety factors. These disadvantages largely outweigh the benefits of pseudo-frictional toughening.

To better understand the benefits associated with fibre modification, the bar charts in Fig. 9 compare the ultimate stress and ER of fibre yarns with and without impregnation, along with the corresponding standard deviation.

In terms of ultimate stress, impregnation affords a 50% gain over the as-received yarn, with a remarkable increase in the exploitation ratio, which exceeds 80% of the fibre's potential. This outcome for MPF occurs with little increase in data scatter and should be compared with the original 55% *ER* offered by as-received PF yarns. It is worth emphasising that the nominal 100% *ER* for yarns is virtually unattainable due to the uneven traction of the fibres in a bundle [58].

Fig. 10 displays the typical failure mode for both groups of samples. It clearly reveals that the failure of non-impregnated yarns is governed by sliding friction of the core filaments after complete debonding from the surrounding matrix. Stresses are only transferred by the few sleeve fibres.

In this regard, optical magnification (top right inlet) indicates that sleeve filaments fail one after the other under tension, owing to uneven stress distribution and are no longer aligned with the core filaments, as a consequence of telescopic unfolding. In addition, the sleeve filaments appear to be damaged by friction. On the other hand, impregnated

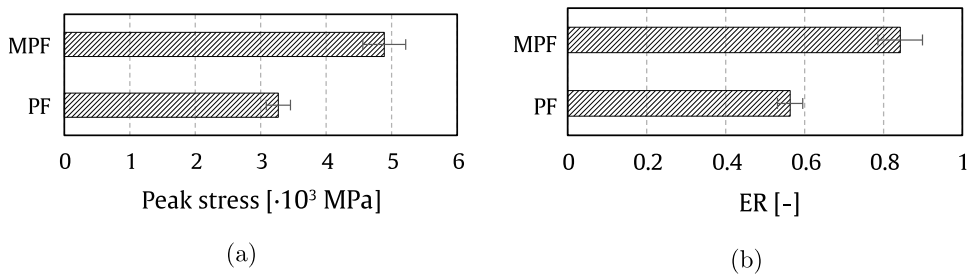

Fig. 9. Effect of mineral impregnation on the ultimate strength (a) and on the exploitation ratio (ER) of PBO yarns (b), alongside the relevant standard deviation bars.

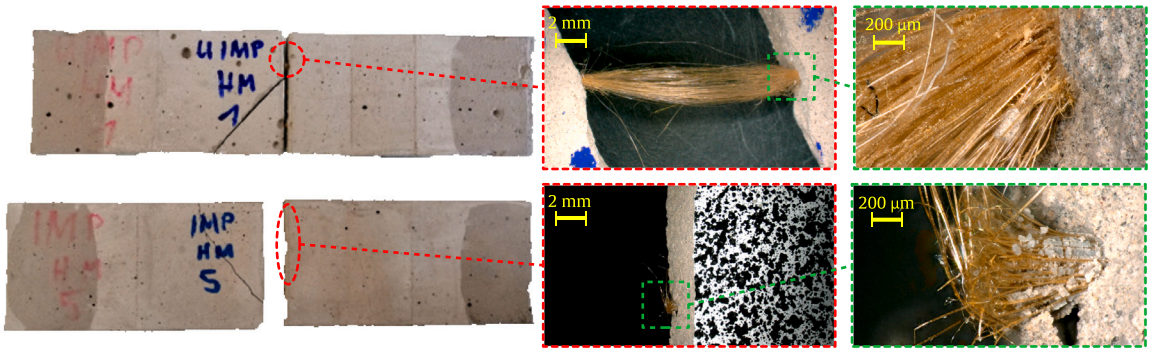

Fig. 10. Typical failure modes for non-impregnated (PF, top) and mineral-impregnated (MPF, bottom) specimens. From left to right: specimen blocks are separated after failure, the connecting filaments having being extracted (top) or ruptured (bottom), the difference clearly appearing under optical magnification.

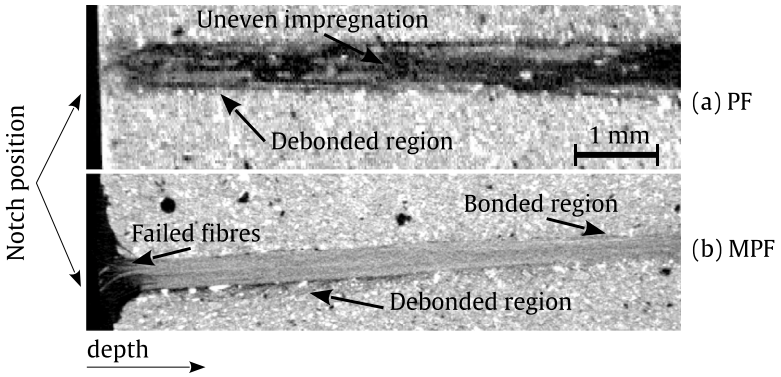

Fig. 11. μCT scans after failure.

yarns fail abruptly in rapid succession, as documented by the three stress drops in each of the curves in Fig. 8b. In particular, the magnified inlet of Fig. 10 (bottom right) reveals fragments of the original impregnation, severely damaged by friction, still attached to the filaments. Indeed, the impregnation is likely to act as a fibre protection during mechanical testing.

The yarn-matrix interface after failure is analysed in Fig. 11 by using micro-computed tomography scans, which provide additional information on the mechanical behaviour of the two groups along the yarn direction.

Dark areas represent either air or very low density materials, while the mineral binder appears with high brightness. As individual PBO filaments are very thin and close to the resolution of the µCT scanner, they cannot be clearly seen. However, the yarn and its connection to the surrounding matrix can be well appreciated. In particular, the outer boundary of non-impregnated PF yarns appears blurred and undefined, as they are surrounded by voids or randomly distributed mortar residues. In fact, it can be argued that a continuous crack has propagated along the length of the fibre from the notch cross-section well into the matrix. Conversely, the impregnated yarn boundaries clearly stand out as they remain well embedded in (and defined by) the fine-grained mortar. Most remarkably, a debonding region with clear evidence of fibre rupture can be plainly identified in the vicinity of the notch. As envisaged in the discussion of the pull-out curves, debonding appears to affect only a fraction of the yarn length. This evidence reveals that the bond is significantly improved by impregnation and therefore the tensile strength of the yarn is the limiting factor for these particular test conditions.

4. Mechanical modelling

In this section, the pull-out response of PBO fibre yarns is interpreted through a one-dimensional mechanical model with the aim of quantitatively assessing the role of the impregnation in promoting adhesion to the matrix. For simplicity, the fibre-matrix interaction is described as an exchange of shear stresses in a simple framework that is constructed according to the general principles described in Kerans and Parthasarathy [42]. Since the full model derivation lies beyond the scope of this paper, only a general overview is hereinafter presented.

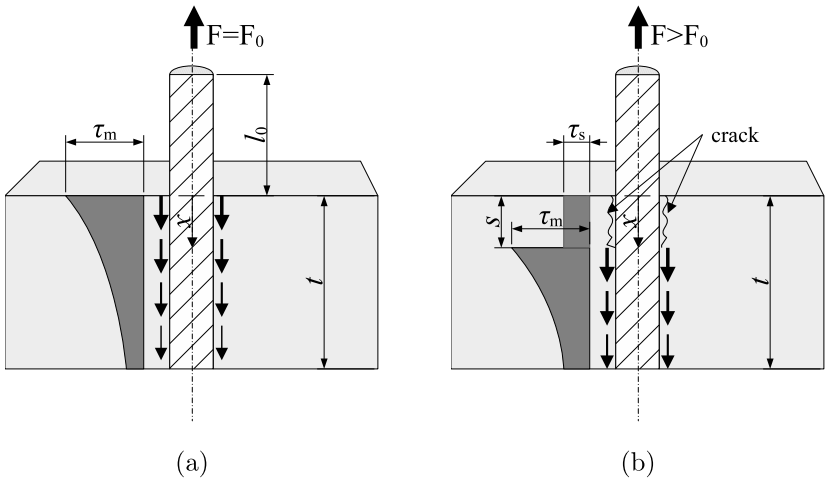

Fig. 12. Schematics of a fibre embedded in a matrix with embedment length t. The applied force F is transmitted to the matrix through the shearing force distribution (Eq. (1)), until $F = F_0$ and the maximum shear force $\tau_m = \eta\tau_s$ is reached (a). Beyond this point, debonding develops (b) over the length $s < t$ with frictional shear $\tau_s < \tau_m$. Softening kicks in at $F = F_1$, when $\tau(t) = \tau_s$.

In this 1-D model, the fibre is embedded in the matrix with length t, starting from $x = 0$, so that $0 \le x \le t$, and it is acted upon by the extraction force $F > 0$ (Fig. 12). From the reference configuration, a linear response gradually develops $u = \frac{F}{EA} l_0$, where l_0 is the free length of the fibre extruding from the matrix, E and A are the Young's modulus and the cross-sectional area of the fibre, respectively. Following a standard approach, it is assumed that the shear stress τ within the matrix follows an exponential law

$$\tau(x) = \tau_0 \exp(-\chi x), \quad \chi > 0, \tag{1}$$

where χ is the decay rate, that is related to the extinction length, and $\tau_0 = \tau_0(F)$ is a monotonically increasing function of the applied force F. This behaviour stands for $F \le F_0$ and $u \le u_0$, equality holding when the maximum shear stress that can be exchanged with the matrix, τ_m, is locally attained, namely $\tau_0(F_0) = \tau_m$. Beyond this point, debonding occurs, either progressively or catastrophically, so that the exponential stress distribution moves deeper into the matrix, starting from $x = s$, with $0 < s < t$. Besides, frictional interaction between fibre and matrix develops in the range $0 < x < s$, in the form of a constant shear $\tau_s = \tau_m/\eta$, i.e.

$$\tau(x) = \begin{cases} \tau_s, & x < s, \\ \eta\tau_s \exp(-\chi x/t), & s \le x \le t \end{cases} \tag{2}$$

It is important to emphasise that, although, in principle, it is possible to assume $\eta < 1$, this condition is ruled out on the basis that debonding occurs by interface weakening. When $\eta > 1$, the force required to further press debonding is monotonically increasing (at least initially) and hardening occurs. Consequently, catastrophic failure right after the linear regime is ruled out, which conforms to the experimental evidence presented here (see Fig. 8). The maximum pull-out force $F_1 > F_0$ is attained when

$$\tau(t) = \tau_s, \tag{3}$$

whence $s = s_1 = t - \chi^{-1} \ln\eta$. The corresponding displacement is labelled u_1 and it can be equally calculated. It is convenient to introduce the dimensionless coordinate $\zeta = x/t$ and the dimensionless decay rate $\kappa = \chi t$. Then

$$\zeta_1 = s_1/t = 1 - \kappa^{-1} \ln\eta, \tag{4}$$

provided

$$1 \le \eta \le \exp\kappa. \tag{5}$$

The corresponding load curve displays hardening up to peak load F_1. Beyond this point, softening kicks in, associated with complete fibre debonding and slippage. This new regime is dominated by dynamic friction and it is not considered here. Within this interpretation, the load curve can be divided into three main branches, namely the linear, the hardening and the softening regimes. In particular, the hardening regime may be singled out by removing the linear part of the curve, for $u < u_0$, and then considering the load ratio F/F_0, which expresses the additional force demanded after the linear regime. In our model, this ratio can be approximated by the expression

$$F/F_0 = f(\zeta) = \frac{e^\kappa(\zeta\kappa + \eta) - \eta e^{\zeta\kappa}}{\eta(e^\kappa - 1)}, \tag{6}$$

where only two parameters, namely η and κ, appear. The corresponding expression for the displacement is much more involved as it requires the setting of important material parameters related to the fibre stiffness, cross-sectional area and free length l_0, which are inherently difficult to assess in the current experimental setup. For this reason, the simplifying assumption that displacement is a linear function of force is made and the analysis is restricted to the load curve. The curve $f(\zeta)$, that is simply defined by the parameter pair η and κ, exhibits a maximum point located at

$$\zeta_m = \kappa^{-1} \ln\left(\eta^{-1} \exp\kappa\right). \tag{7}$$

In the light of (5), it is $0 \le \zeta_m \le 1$. It is now possible to determine the parameters κ and η by imposing two conditions, namely that

1. the maximum point is given by

$$f(\zeta_m) = F_1/F_0, \tag{8}$$

2. and the dimensionless area under the F/F_0 curve up to the maximum point reads

$$A_1 = \int_0^{\zeta_m} f(\zeta)\mathrm{d}\zeta = \frac{e^\kappa\left(\zeta_m^2\kappa^2 + 2\eta\zeta_m\kappa - 2\right) + 2\eta}{2\eta(e^\kappa - 1)\zeta_m\kappa}. \tag{9}$$

In particular, the first condition is typical of the study of strength curves, where the maximum is often considered to be the cracking stress, while the second is related to the energy dissipated in the delamination process.

4.1. Data fitting

The initial step in data fitting involves removing undesired fluctuations and noise from the experimental curves, which can blur the underlying trend. This is achieved by taking a 10-neighbour mean of each individual data point.

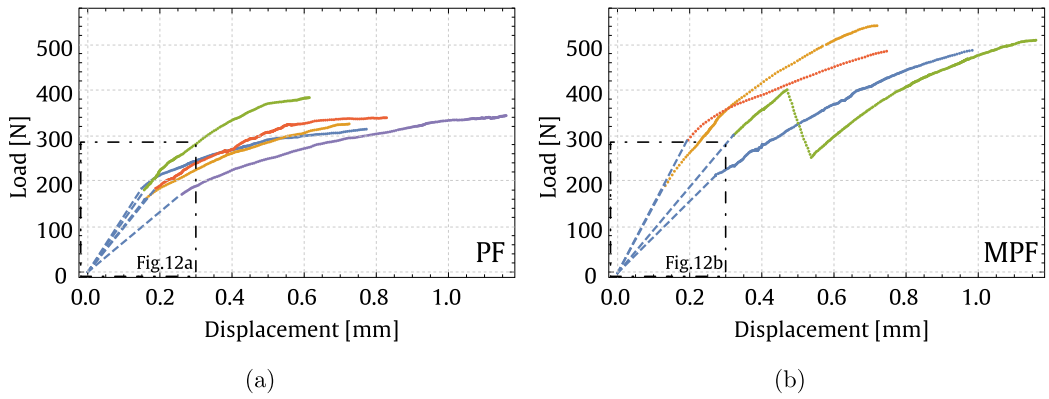

Fig. 13. Linear fit (dashed) up to (u_0, F_0) and post-linear filtered data (solid) for uncoated (a) and coated (b) fibres, up to the peak load F_1 and displacement u_1. It is observed that a sudden load drop occurs in one specimen in the coated group, likely due to fibre failure.

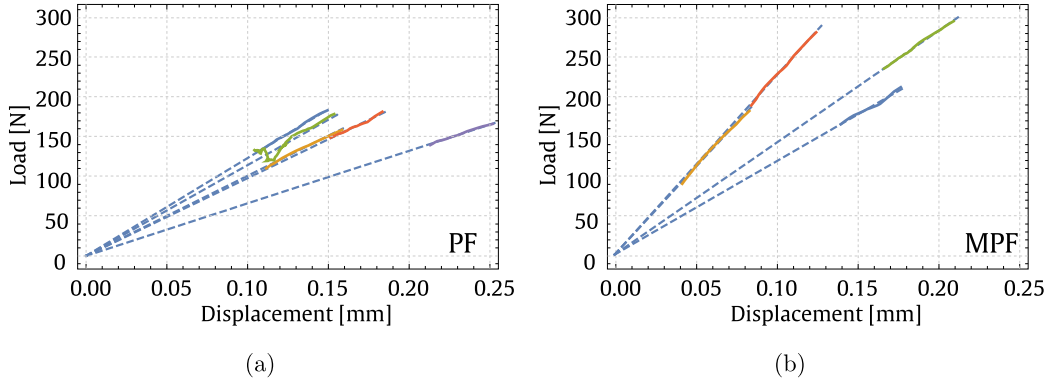

Fig. 14. Linear fit (dashed) plotted over the filtered data set (solid curve) for each specimen in the linear regime. Very small displacement values have been removed because they are strongly affected by setup imperfections.

Subsequently, the linear regime is captured by fitting, through the least square method, a linear approximant onto the experimental curve in a given force range $F < F_0$, namely

$$F = E_t u + d. \tag{10}$$

In this process, the yarn stiffness, E_t, and displacement offset, d, are estimated, the latter being the precise amount of shift required to uniformly align data points to have zero intercept with the load axis (i.e. zero force at zero displacement, as in Fig. 13). Clearly, E_t becomes a proper Young modulus provided that F is scaled by the yarn cross-section and u by a reference length, say l_0. Since these quantities are difficult to determine (and generally vary), we prefer to adopt E_t as the most reliable expression for the stiffness of the yarn. The resulting fit, up to F_0, is shown as a dashed line in Fig. 13, and it is followed, from F_0 to F_1, by the hardening part of the load curve (solid in the Figure). The quality of the fit is illustrated in Fig. 14 and it is generally very satisfactory, apart from one specimen in the PF group that exhibits erratic behaviour already in the linear regime. Fitting parameters are gathered in Table 6.

Once the linear regime is captured, the spotlight is moved to the debonding process occurring in the hardening regime, until the maximum load F_1 is reached. Precisely this part of the experimental curve, brought in dimensionless form by dividing the load $F_0 < F < F_1$ by the maximum linear load F_0, is fitted onto the model response, given by (Eq. (6)) and the parameter pair η, κ is obtained. Again, fitting is accomplished by the least square method, yet this time under the following constraints:

1. $\eta < \exp\kappa$, $\kappa > 0$;
2. the area under the curve in the hardening regime obtained from the dataset corresponds to Eq. (9);
3. the bond quality affects κ and η simultaneously, therefore it is demanded that $\eta > 1 + \kappa/10$.

The last constrain is physically and numerically motivated. From a physical standpoint, it expresses the expectation that better adhesion to the matrix entails a higher maximum shear stress τ_m and a shorter extinction length χ^{-1}. Numerically, these constraints prevent the fitting algorithm from hitting the boundaries of the optimisation region for one parameter and then seeking the optimum value of the other.

Whenever load drops, that emerge in the load curve as jumps originating from the unexpected and premature failure of a single yarn, are observed, as it is the case in one impregnated specimen only, they are disregarded, i.e. the curve is patched together. Considering specimen 2 in the PF group as an example, Fig. 15 shows the hardening curve load data superposed to the non-linear fit to the model (6), alongside the residual curve.

It appears that the residuals are very small and the fit is extremely accurate. It can also be observed that the experimental strength curve approaches the maximum value F_1 with a vanishing slope. The quality of the approximation can be better appreciated from the fitting parameters, which are collected in Table 6 alongside a measure of their effectiveness, for all the specimens in both the PF and MPF groups. Indeed, the parameters are given together with the standard error, which is generally small.

The notable exceptions are sample 3 in the PF group and sample 1 in the MPF group (in parenthesis), both of which appear to be far from the trend, although in different ways. Specifically, the former presents a poor quality of the linear fit at small displacements and shows unexpected wiggles in the load curve, most likely due to experimental uncertainty. In contrast, MPF specimens are most likely to fail by fibre rupture and, in this sense, the parameters η and κ reflect this different

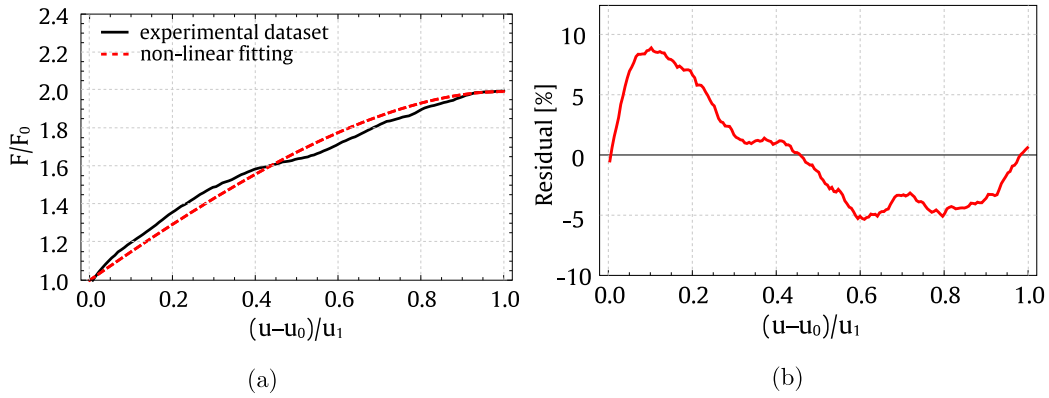

Fig. 15. (a) F/F_0 dataset (solid, black) for a representative specimen (#2) in the PF group superposed onto the non-linear fit (6) (dashed, red). In the inlet (b), the plot of the interpolation residuals (i.e. the difference between the measured and the interpolated values) is displayed.

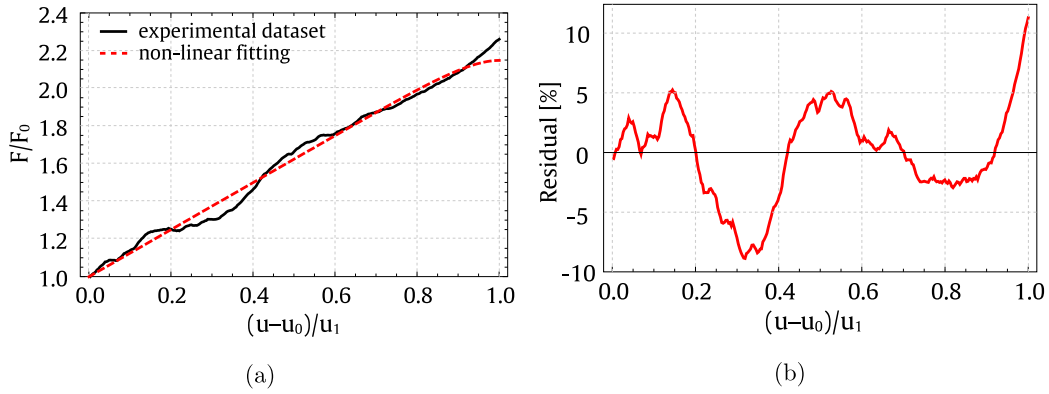

Fig. 16. (a) F/F_0 dataset (solid, black) for specimen 1 in the MPF group superposed onto the non-linear fit (6) (dashed, red). In the inlet (b), the plot of the interpolation residuals (i.e. the difference between the measured and the interpolated values) is shown.

Table 6
Fitting parameters η and κ of the load ratio F/F_0 in the Hardening regime, for each specimen in the non-impregnated (PF) and impregnated (MPF) groups.

PF	sp1	sp2	(sp3)	sp4	sp5	Mean[a]
η	1.15	1.21	13.23	1.18	1.25	**1.20**
std. err.	0.21	0.17	4.25	0.07	0.23	CoV 3.5%
κ	1.48	2.09	18.64	1.79	2.46	**1.96**
std. err.	0.44	0.39	5.37	0.17	0.56	CoV 21%
MPF	(sp1)	sp2	sp3	sp4		Mean[a]
η	9.87	1.97	1.25	1.84		**1.69**
std. err.	1.08	0.25	0.11	0.30		CoV 22%
κ	14.63	5.30	2.53	2.54		**3.46**
std. err.	1.41	0.64	0.29	0.42		CoV 46%

[a] Clearly, specimen 3 in the PF group and specimen 1 in the MPF group are well off the data distribution and therefore they are disregarded in the means.

Table 7
Mechanical parameters: comparison between the non-impregnated (PF) and impregnated (MPF) groups. $F_{0,1}$ load at the end of the linear (hardening) regime and corresponding elongation $u_{0,1}$. A_1 is the dimensionless area under the curve in the hardening regime and E_t the yarn stiffness in the linear regime.

Parameter [unit]	PF		MPF		Δ%
	Mean	CoV	Mean	CoV	
E_t [$\frac{N}{mm}$]	1004	21%	1811	31%	74%
F_0 [N]	176	6%	250	21%	42%
u_0 [mm]	0.08	–	0.08	–	–
F_1 [N]	341	8%	507	5%	49%
u_1 [mm]	0.72	22%	0.52	16%	−28%
A_1 [–]	1.58	7%	1.71	17%	8%

pattern. However, for most specimens, fibre rupture takes place very close to the initiation of fibre pull-out. In fact, as already discussed, the load drop due to fibre rupture still generally occurs when the slope of the load curve is very small.

In this regard, specimen 3 in the MPF group is a noteworthy exception as it features a non-convex behaviour to the maximum load, which occurs prior to a major load drop. Fig. 16 illustrates this behaviour as well as the residual plot. Accordingly, the exceedingly high values of κ and η provide best evidence of clear fibre rupture. For these reasons, such specimens have been excluded from the mean in Table 6.

4.2. Discussion

Table 7 compares the key mechanical properties emerging from the tests. In particular, it shows that impregnation determines significant gains in stiffness and strength over the PF group, both in the linear and hardening regimes. As it is often the case, the increase in peak force F_1 comes at the expense of the corresponding displacement u_1, that is reduced by 28%. Nevertheless, toughness A_1 is significantly improved in the linear regime, and also somewhat improved in the hardening regime. Deformation is reduced in the post-linear regime, but the gain in strength outweighs this loss in terms of mechanical energy absorbed by the system.

By examining the model parameters collected in Table 6, it is evident that impregnation leads to a 41% increase in η with respect to the PF group. This gain is very close to the corresponding increase

in F_0, as per Table 7. This observation suggests that the interface strength enhancement given by fibre impregnation is mostly effective in the linear regime and it specifically affects τ_m, i.e. the maximum shear stress which can be transferred to the matrix. However, the same improvement does not extend to the pull-out process, and in fact, it appears that the friction shear load τ_s is the same in the PF and MPF groups. Looking at κ, no clear trend can be identified, also on account of the limited number of specimens. Still, the mean value in the MPF group shows a 77% increase over the PF group. This implies that the enhanced interface transfers shear stress from the yarn to the matrix much more efficiently, hence the extinction length is greatly reduced. This has important positive effects on the anchoring length, which also significantly reduces.

Finally, a notable covariance effect in terms of data scattering is observed, whereby higher performance is accompanied by larger data deviation. Still, especially considering the small sample size, data scattering appears good in the PF group, and acceptable in the MPF group. More extensive testing with larger data sets and at different embedment lengths are advocated to better assess the extent of the interface enhancement.

5. Conclusions

This paper presents the experimental characterisation of the bond quality of PBO multifilament yarns embedded in a newly developed limestone calcined clay (LC^3) cement mortar. Spotlight is set on the assessment of the performance improvement achieved by cement-based impregnation of the PBO yarns, with particular emphasis on the yarn-matrix interaction. To this aim, double sided pull-out tests are conducted alongside non-destructive investigations, such as optical and scanning electron microscopy as well as micro-computed tomography. An analytical one-dimensional cohesive mechanical model, based on crack propagation and friction, is adopted to interpret the experimental curves and to pinpoint the contribution of mineral impregnation of the multifilament yarn. In summary, the following conclusions can be outlined:

- Bare PBO fibres demonstrate weak adhesion with the surrounding matrix and, consequently, they exhibit the usual mechanical response associated with this condition, namely early extraction and friction-dominated failure with strong evidence of telescopic failure, whereby the core filaments slide over the sleeve, i.e. the outer filaments. This response is associated with large data scattering and poor conversion (i.e. exploitation) of the fabric potential.
- In contrast, cement impregnation effectively penetrates the PBO fibre bundles, owing to the abundance of fine cement particles, designed to bind the individual filaments together into a monolithic thin rod, thus preventing differential sliding.
- Mineral impregnation is also important as it greatly improves the interface bond with the matrix, delaying yarn full debonding and reducing data scattering. Ultimately, mineral impregnation leads to remarkable improvement in the exploitation extent of the tensile properties of the PBO fabric.
- Consequently, the failure mode shifts significantly for impregnated PBO fibres and most often reaches fibre rupture (although on the verge of complete debonding), in the shape of successive stress drops until sudden failure occurs. As it is usually the case, this hardening mechanical response is achieved at the expense of elongation and ductility, yet in an overall favourable balance for toughness (i.e. absorbed energy). In fact, telescopic failure is characterised by large elongation ductility in a markedly softening response.
- Despite the limited sample size, the analytical model nicely captures the essential features of the mechanical system. Indeed, it reveals that the maximum shearing force that can be transferred to the matrix is strongly affected by impregnation. This effect is consistent across both linear and non-linear regimes. On the contrary, the frictional shear stress remains unaffected by impregnation. Furthermore, higher shear stress results in decreased extinction (and anchoring) length.
- The model also identifies different failure modes, a significant increase in linear elastic stiffness (Young's modulus) linked to tension-stiffening, and a reduction in elongation ductility, while toughness improves slightly.

This investigation provides promising evidence in the direction of manufacturing a wide variety of uniaxial and multiaxial strengthening meshes for textile-reinforced concrete (TRC) systems made from mineral impregnated PBO yarns. Such systems, taking advantage of the excellent strength and toughness properties demonstrated by mineral-impregnated PBO yarns, in a cost-effective impregnation technology, may finally match the performance of well established FRP solutions in the field of externally-applied strengthening systems, while offering superior qualities in terms of durability, temperature resistance and reversibility. This new technology may especially meet the demands of delicate structural applications such as impact strengthening of concrete members.

List of symbols

l_0	Length of the yarn emerging from the matrix
t	Yarn embedment (anchoring) length in the matrix
$0 < x < t$	Axial coordinate alongside the yarn inside the matrix
$0 < s < t$	Crack length, i.e. $x < s$ is the crack zone, where $\tau = \tau_s$, $s < x < t$ is the uncracked zone where τ is given by (1)
F_0, u_0	Force and displacement in the pull-out test at the limit of the linear regime
E_t	Yarn stiffness in the linear regime, related to Young's modulus of the yarn
F_1, u_1	Peak force and corresponding displacement in the pull-out test
$\tau_m = \eta\tau_s$	Maximum shear stress which is supported by the undamaged matrix
τ_s	Shear stress supported by the damaged (cracked) matrix
$\chi = \kappa t^{-1}$	Exponential decay rate for the stress in the undamage matrix, closely related to the extinction length L_e
A_1	(dimensionless) area under the F/F_0 vs. $\zeta = x/t$ curve in the hardening regime (ratio of the hardening toughness over the stored elastic energy)

Funding

The financial support of the German Research Foundation (Deutsche Forschungsgemeinschaft, DFG) in the framework of the Research Training Group (Graduiertenkollegs, GRK) 2250, entitled "*Mineral-bonded composites for enhanced structural impact safety*" (grant no. 287321140) is gratefully acknowledged. ML acknowledges financial support under the long-term visiting program by the University of Modena and Reggio Emilia. AN and CS are also grateful to the Italian National Group of Mathematical Physics (GNFM), and specifically CS was supported by the Young Researcher scheme 2020 (Approved by Prot. U-UFMBAZ-2021-000072).

CRediT authorship contribution statement

Cesare Signorini: Writing – review & editing, Writing – original draft, Visualization, Validation, Supervision, Methodology, Investigation, Data curation, Conceptualization. **Andrea Nobili:** Writing – review & editing, Writing – original draft, Methodology, Investigation, Formal analysis, Conceptualization. **Marco Liebscher:** Writing

– review & editing, Supervision, Methodology, Investigation, Conceptualization. **Jitong Zhao:** Investigation. **Ameer H. Ahmed:** Investigation. **Thomas Köberle:** Investigation. **Viktor Mechtcherine:** Writing – review & editing, Supervision, Resources, Funding acquisition.

Declaration of competing interest

The authors declare that they have no known competing financial interests or personal relationships that could have appeared to influence the work reported in this paper.

Data availability

Data will be made available on request.

Acknowledgements

The Authors would like to thank Dr.-Ing. Marko Butler for the fruitful discussions, Mr Christian Stahn, Mr Nicholas Winkler and Ms Anna Jose for their valuable support with specimen preparation, and Mr Kai-Uwe Mehlisch for technical assistance with the tests.

References

[1] Mechtcherine V. Novel cement-based composites for the strengthening and repair of concrete structures. Constr Build Mater 2013;41:365–73.
[2] Koutas LN, Tetta Z, Bournas DA, Triantafillou TC. Strengthening of concrete structures with textile reinforced mortars: State-of-the-art review. J Compos Constr 2019;23(1):03118001. http://dx.doi.org/10.1061/(ASCE)CC.1943-5614.0000882.
[3] Alecci V, De Stefano M, Focacci F, Luciano R, Rovero L, Stipo G. Strengthening masonry arches with lime-based mortar composite. Buildings 2017;7(2):49.
[4] Ferretti F, Tilocca AR, Incerti A, Mazzotti C, Savoia M. Effects of thermal variations on the tensile behavior of FRCM strengthening systems. J Compos Constr 2022;26(5):04022067.
[5] Kitagawa T, Murase H, Yabuki K. Morphological study on poly-p-phenylenebenzobisoxazole (PBO) fiber. J Polym Sci B: Polym Phys 1998;36(1):39–48.
[6] Davies P, Bunsell AR, Chailleux E. Tensile fatigue behaviour of PBO fibres. J Mater Sci 2010;45:6395–400.
[7] Al-Lami K, D'Antino T, et al. Durability of fabric-reinforced cementitious matrix (FRCM) composites: A review. Appl Sci 2020;10(5):1714.
[8] Signorini C, Nobili A. Comparing durability of steel reinforced grout (SRG) and textile reinforced mortar (TRM) for structural retrofitting. Mater Struct 2021;54(3):1–15.
[9] Curosu I, Liebscher M, Burk S, Li H, Hempel S, Raak N, Rohm H, Mechtcherine V. Influence of fiber type on the tensile behavior of high-strength strain-hardening cement-based composites (SHCC) at elevated temperatures. Mater Des 2021;198:109397.
[10] Trapko T, Musiał M. Effect of PBO–FRCM reinforcement on stiffness of eccentrically compressed reinforced concrete columns. Materials 2020;13(5):1221.
[11] Trapko T, Rogalski K, Musiał M, Ombres L. Effectiveness of concrete elements strengthening through PBO-FRCM confinement with various types of anchorage. J Mater Civ Eng 2021;33(1):04020409, Publisher: American Society of Civil Engineers.
[12] Ombres L. Flexural analysis of reinforced concrete beams strengthened with a cement based high strength composite material. Compos Struct 2011;94(1):143–55.
[13] Marcinczak D, Trapko T, Musiał M. Shear strengthening of reinforced concrete beams with PBO-FRCM composites with anchorage. Composites B 2019;158:149–61.
[14] Di Tommaso A, Focacci F, Mantegazza G, Gatti A. FRCM versus FRP composites to strengthen RC beams: a comparative analysis. In: Proceedings of the international symposium on fibre reinforced polymers for reinforced concrete structures (FRPRCS8). Patras, Greece. 2007.
[15] Carloni C, Mazzotti C, Savoia M, Subramaniam KV. Confinement of masonry columns with PBO FRCM composites. In: Key Engineering Materials, Vol. 624, Trans Tech Publ; 2015, p. 644–51.
[16] Alecci V, Focacci F, Rovero L, Stipo G, De Stefano M. Extrados strengthening of brick masonry arches with PBO–FRCM composites: Experimental and analytical investigations. Compos Struct 2016;149:184–96.
[17] D'Ambrisi A, Focacci F, Caporale A. Strengthening of masonry–unreinforced concrete railway bridges with PBO-FRCM materials. Compos Struct 2013;102:193–204.
[18] Curosu I, Liebscher M, Mechtcherine V, Bellmann C, Michel S. Tensile behavior of high-strength strain-hardening cement-based composites (HS-SHCC) made with high-performance polyethylene, aramid and PBO fibers. Cem Concr Res 2017;98:71–81.
[19] D'Antino T, Calabrese AS, Colombi P, Poggi C. Experimental and numerical investigation on the tensile behavior of PBO FRCM composites with textile lap splice. Constr Build Mater 2023;363:129437.
[20] Valeri P, Ruiz MF, Muttoni A. Tensile response of textile reinforced concrete. Constr Build Mater 2020;258:119517.
[21] Banholzer B, Brockmann T, Brameshuber W. Material and bonding characteristics for dimensioning and modelling of textile reinforced concrete (TRC) elements. Mater Struct 2006;39(8):749–63.
[22] Donnini J, y Basalo FDC, Corinaldesi V, Lancioni G, Nanni A. Fabric-reinforced cementitious matrix behavior at high-temperature: Experimental and numerical results. Composites B 2017;108:108–21.
[23] Signorini C, Nobili A, Falope FO. Mechanical performance and crack pattern analysis of aged carbon fabric cementitious matrix (CFRCM) composites. Compos Struct 2018;202:1114–20.
[24] Guo S, Ren J, Yang T, Rahman MZ, Shi C, Zhu D. Influences of surface treatment on the mechanical performances of carbon and basalt textiles-reinforced concretes under harsh environments. Composites B 2022;246:110195.
[25] Cohen Z, Peled A. Effect of nanofillers and production methods to control the interfacial characteristics of glass bundles in textile fabric cement-based composites. Composites A 2012;43(6):962–72.
[26] Nadiv R, Peled A, Mechtcherine V, Hempel S, Schröfl C. Micro-and nanoparticle mineral coating for enhanced properties of carbon multifilament yarn cement-based composites. Composites B 2017;111:179–89.
[27] Signorini C, Nobili A. Targeting functionalised carbon nanotubes at the interphase of textile reinforced mortar (TRM) composites. Composites A 2021;144:106330.
[28] Li H, Liebscher M, Michel A, Quade A, Foest R, Mechtcherine V. Oxygen plasma modification of carbon fiber rovings for enhanced interaction toward mineral-based impregnation materials and concrete matrices. Constr Build Mater 2021;273:121950.
[29] Signorini C, Sola A, Malchiodi B, Nobili A. Highly dissipative fiber-reinforced concrete for structural screeds. J Mater Civ Eng 2022;34(4):04022022.
[30] Schneider K, Lieboldt M, Liebscher M, Fröhlich M, Hempel S, Butler M, Schröfl C, Mechtcherine V. Mineral-based coating of plasma-treated carbon fibre rovings for carbon concrete composites with enhanced mechanical performance. Materials 2017;10(4):360.
[31] Schneider K, Michel A, Liebscher M, Terreri L, Hempel S, Mechtcherine V. Mineral-impregnated carbon fibre reinforcement for high temperature resistance of thin-walled concrete structures. Cem Concr Compos 2019;97:68–77.
[32] Zhao J, Liebscher M, Michel A, Junger D, Trindade ACC, de Andrade Silva F, Mechtcherine V. Development and testing of fast curing, mineral-impregnated carbon fiber (MCF) reinforcements based on metakaolin-made geopolymers. Cem Concr Compos 2021;116:103898.
[33] de Castro Silva RM, Zhao J, Liebscher M, Curosu I, de Andrade Silva F, Mechtcherine V. Bond behavior of polymer-and mineral-impregnated carbon fiber yarns towards concrete matrices at elevated temperature levels. Cem Concr Compos 2022;133:104685.
[34] Zhao J, Zhao D, Liebscher M, Yin B, Mohammadi M, Butler M, Köberle T, Kaliske M, Mechtcherine V. Temperature-dependent pullout behavior of geopolymer concrete reinforced with polymer-or mineral-impregnated carbon fiber composites: An experimental and numerical study. ACS Sustain Chem Eng 2023.
[35] Mechtcherine V, Michel A, Liebscher M, Schneider K, Großmann C. Mineral-impregnated carbon fiber composites as novel reinforcement for concrete construction: Material and automation perspectives. Autom Constr 2020;110:103002.
[36] Liebscher M, Zhao J, Wilms G, Michel A, Wilhelm K, Mechtcherine V. Influence of roller configuration on the fiber–matrix distribution and mechanical properties of continuously produced, mineral-impregnated carbon fibers (MCFs). Fibers 2022;10(5):42.
[37] Kelly A. Interface effects and the work of fracture of a fibrous composite. Proc R Soc Lond Ser A Math Phys Eng Sci 1970;319(1536):95–116.
[38] Hutchinson JW, Jensen HM. Models of fiber debonding and pullout in brittle composites with friction. Mech Mater 1990;9(2):139–63.
[39] Sorzia A, Lanzoni L, Radi E. Pullout modelling of viscoelastic synthetic fibres for cementitious composites. Compos Struct 2019;223:110898.
[40] Sorzia A, Signorini C, Volpini V, Di Maida P. Analytical approach for modelling the pull-out mechanism of recycled synthetic fibres in fibre-reinforced concrete (FRC). Key Eng Mater 2022;919:35–46.
[41] DiFrancia C, Ward TC, Claus RO. The single-fibre pull-out test. 1: Review and interpretation. Composites A 1996;27(8):597–612.
[42] Kerans RJ, Parthasarathy TA. Theoretical analysis of the fiber pullout and pushout tests. J Am Ceram Soc 1991;74(7):1585–96.
[43] DiFrancia C. The single fiber pull-out test: a study of fiber/matrix interactions (Ph.D. thesis), Virginia Tech; 1992.
[44] Zhou P, Feng P. Unified analysis for tailorable multi-scale fiber reinforced cementitious composites in tension. Composites B 2023;254:110586.

[45] Toyobo MC Corporation Ltd. Zylon® (PBO fiber) technical information. 2005, https://www.toyobo-global.com/seihin/kc/pbo/zylon-p/bussei-p/technical_201118.pdf Accessed: 2023-07-24.
[46] Huang Y, Frings P, Hennes E. Mechanical properties of Zylon/epoxy composite. Composites B 2002;33(2):109–15.
[47] Scrivener K, Favier A, et al. Calcined clays for sustainable concrete. Springer; 2015.
[48] Zhou Y, Gong G, Xi B, Guo M, Xing F, Chen C. Sustainable lightweight engineered cementitious composites using limestone calcined clay cement (LC^3). Composites B 2022;243:110183.
[49] Ahmed AH, Nune S, Liebscher M, Köberle T, Willomitzer A, Noack I, Butler M, Mechtcherine V. Exploring the role of dilutive effects on microstructural development and hydration kinetics of limestone calcined clay cement (LC^3) made of low-grade raw materials. J Clean Prod 2023;428:139438.
[50] Mechtcherine V, Michel A, Liebscher M, Schmeier T. Extrusion-based additive manufacturing with carbon reinforced concrete: Concept and feasibility study. Materials 2020;13(11):2568.
[51] Butler M, Mechtcherine V, Hempel S. Experimental investigations on the durability of fibre–matrix interfaces in textile-reinforced concrete. Cem Concr Compos 2009;31(4):221–31.
[52] ACI PRC-5496-20. Guide to design and construction of externally bonded fabric-reinforced cementitious matrix (FRCM) and steel-reinforced grout (SRG) systems for repair and strengthening masonry structures. American Concrete Institute; 2020.
[53] Portal NW, Perez IF, Thrane LN, Lundgren K. Pull-out of textile reinforcement in concrete. Constr Build Mater 2014;71:63–71.
[54] Slama A-C, Gallias J-L, Fiorio B. Study of the pull-out test of multifilament yarns embedded in cementitious matrix. J Compos Mater 2021;55(2):169–85.
[55] Homoro O, Michel M, Baranger TN. Pull-out response of glass yarn from ettringite matrix: Effect of pre-impregnation and embedded length. Compos Sci Technol 2019;170:174–82.
[56] Yin S, Xu S, Wang F. Investigation on the flexural behavior of concrete members reinforced with epoxy resin-impregnated textiles. Mater Struct 2015;48:153–66.
[57] Signorini C, Sola A, Nobili A. Hierarchical composite coating for enhancing the tensile behaviour of textile-reinforced mortar (TRM). Cem Concr Compos 2023;140:105082.
[58] Broughton Jr RM, Mogahzy Jr YE, Hall Jr D. Mechanism of yarn failure. Text Res J 1992;62(3):131–4.